The Astrophysical Journal, 893:13 (15pp), 2020 April 10 https://doi.org/10.3847/1538-4357/ab734a

Confirmation of Enhanced Long-wavelength Dust Emission in OMC 2/3

Brian Mason[1], Simon Dicker[2], Sarah Sadavoy[3], Sara Stanchfield[2], Tony Mroczkowski[4], Charles Romero[2], Rachel Friesen[1,5], Craig Sarazin[6], Jonathan Sievers[7], Thomas Stanke[4], and Mark Devlin[2]
[1] NRAO—National Radio Astronomy Observatory, 520 Edgemont Road, Charlottesville, VA 22903, USA
[2] Department of Physics and Astronomy, University of Pennsylvania, 209 South 33rd Street, Philadelphia, PA 19104, USA
[3] Harvard-Smithsonian Center for Astrophysics (CfA), 60 Garden Street, Cambridge, MA 02138, USA
[4] ESO—European Southern Observatory, Karl-Schwarzschild-Str. 2, D-85748 Garching b. München, Germany
[5] Department of Astronomy & Astrophysics, University of Toronto, 50 St. George St., Toronto, ON M5S 3H4, Canada
[6] Department of Astronomy, University of Virginia, 530 McCormick Rd., Charlottesville, VA 22904, USA
[7] McGill University, 3600 University Street, Montreal, QC H3A 2T8, Canada
Received 2019 May 9; revised 2020 January 30; accepted 2020 February 4; published 2020 April 8

Abstract

Previous continuum observations from the MUSTANG camera on the Green Bank Telescope (GBT) of the nearby star-forming filament OMC 2/3 found elevated emission at 3.3 mm relative to shorter-wavelength data. As a consequence, the inferred dust emissivity index obtained from modified blackbody dust spectra was considerably lower than what is typically measured on ∼0.1 pc scales in nearby molecular clouds. Here we present new observations of OMC 2/3 collected with the MUSTANG-2 camera on the GBT that confirm this elevated emission. We also present for the first time sensitive 1 cm observations made with the *Ka*-band receiver on the GBT, which also show higher than expected emission. We use these observations—along with *Herschel*, JCMT, Mambo, and GISMO data—to assemble spectral energy distributions (SEDs) of a variety of structures in OMC 2/3 spanning the range 160 μm to 1 cm. The data at 2 mm and shorter are generally consistent with a modified blackbody spectrum and a single value of $\beta \sim 1.6$. The 3 mm and 1 cm data, however, lie well above such an SED. The spectrum of the long-wavelength excess is inconsistent with both free–free emission and standard "Spinning Dust" models for Anomalous Microwave Emission (AME). The 3 mm and 1 cm data could be explained by a flatter dust emissivity at wavelengths shorter than 2 mm, potentially in concert with AME in some regions.

Unified Astronomy Thesaurus concepts: Dust continuum emission (412); Interstellar dust (836); Molecular clouds (1072); Dense interstellar clouds (371); Interstellar filaments (842); Star formation (1569); Protostars (1302)

1. Introduction

OMC 2/3 is the richest known star-forming filament within 500 pc and has been studied extensively at millimeter, submillimeter, and infrared wavelengths (e.g., Johnstone & Bally 1999; Peterson 2005; Nutter & Ward-Thompson 2007; Davis et al. 2009; Sadavoy et al. 2010; Salji et al. 2015; Stutz & Kainulainen 2015; Megeath et al. 2016). These studies generally aim to map the distribution of star formation within OMC 2/3 to determine how the dense core or young star populations relate to the dynamics of the filament, or to determine the characteristics of the filament itself. Thermal dust emission is particularly useful as a tracer of mass in filaments and star-forming regions more generally. Dust is typically assumed to emit thermal radiation with a modified blackbody (MBB) spectrum:

$$I_{\nu,\mathrm{dust}} \propto \frac{\nu^{(3+\beta)}}{\exp(h\nu/kT_\mathrm{d}) - 1}. \quad (1)$$

Here T_d is the dust grain temperature and the dust emissivity index β is determined by physical properties of the dust such as composition and grain size distribution. This model is generally seen to be an excellent description of dust emission at millimeter and submillimeter wavelengths, with typical values $1.5 < \beta < 2.5$ on filament to molecular cloud scales (e.g., Goldsmith et al. 1997; Sadavoy et al. 2013). Observations of diffuse thermal dust emission at long millimeter wavelengths can be challenging due to the relative faintness of the emission, but are appealing because mass determinations from them are less affected by optical depth considerations than those obtained from shorter-wavelength data. In addition, their greater spectral leverage gives greater sensitivity to the physical properties of dust grains, potentially revealing new physical information. These long-wavelength observations have become readily feasible with advances in instrumentation, such as ALMA, and focal plane arrays on large single-dish telescopes.

With this in mind Schnee et al. (2014) combined observations of OMC 2/3 at $\lambda = 3.3$ mm with MUSTANG on the Robert C. Byrd Green Bank Telescope (GBT) with observations at $\lambda = 1.2$ mm from MAMBO at the IRAM 30 m telescope to study the dust emissivity index in the filament on $\lesssim$0.1 pc scales. Schnee et al. (2014, hereafter S14) found surprisingly high 3 mm emission toward regions dominated by thermal dust emission at shorter wavelengths. S14 tentatively attributed this to grain growth in the filaments resulting in a lower value of $\beta \approx 0.9$. Subsequent analysis (Sadavoy et al. 2016) used *Herschel* submillimeter telescope data at 160–500 μm, as well as 2 mm data from GISMO on the IRAM 30 m. Sadavoy et al. (2016, hereafter S16) measured β values of ∼1.7 on 0.1 pc scales. These values are more consistent with the typical indices found with *Planck* (Planck Collaboration et al. 2015) for molecular clouds, and suggest that the dust grains on OMC 2/3 are not unusually large. S16 showed that the β values in S14 may have been low due to a break in the dust SED at $\lambda > 2$ mm, such that the 3 mm emission appeared to be elevated.

In the course of commissioning the new 3.3 mm MUSTANG-2 camera on the GBT we obtained a 60 minute observation of OMC 2/3. The results of these observations, as well as new 1 cm continuum data from the GBT, are presented

here. MUSTANG-2 is more sensitive than the original MUSTANG camera. Of particular significance to the interpretation of these data is the fact that it has a much larger field of view (FOV; 4.′25 versus 42″). The larger FOV enables much more straightforward reconstruction of extended, diffuse signals and thus provides a valuable cross-check on the results of S14, the achievement of which required a sophisticated, iterative reconstruction algorithm. As a point of comparison MUSTANG-2 readily measures spatial scales six times larger than can currently be measured by ALMA in the continuum at these wavelengths.

The structure of this paper is as follows. Section 2 presents our new 3.3 mm and 1 cm observations of OMC 2/3. Section 3 describes the analysis leading to multi-wavelength SEDs for a variety of structures in the region, and Section 4 considers several possible physical interpretations of them. Finally, Section 5 reviews and presents our conclusions. Except when stated, all error bars indicate 1σ (68% confidence) uncertainties on the quantity of interest.

2. Observations

2.1. MUSTANG-2

MUSTANG-2 is a 215 pixel feedhorn coupled Transition Edge Sensor (TES) bolometer array with a bandpass of 75–105 GHz, corresponding to $\lambda \sim 3.3$ mm. The receiver is cooled with a pulse tube and closed cycle Helium 4/Helium 3 refrigerator, which cools the array to 300 mK. More information on the MUSTANG-2 receiver can be found in Dicker et al. (2014) and Stanchfield et al. (2016).

Observations of OMC 2/3 were acquired in two observing sessions in 2016 December. The data comprise eight individual scans, each approximately 8 minutes in duration, centered on five pointing centers chosen to cover the "integral-shaped filament" in OMC 2/3. Each scan covers a circular area approximately 6.′5 in diameter. The data were calibrated and imaged by a suite of software tools developed by the instrument team in IDL. The time-ordered data were visually inspected for data quality and a small fraction of detectors manually flagged, supplementing automatic detector flags inferred and applied by the calibration software. Local pointing corrections were derived and applied at the map-making stage using bracketing observations of the nearby pointing source J0530+135. Flux density calibration was performed using an observation of 3C84, one of the sources that ALMA regularly monitors (Fomalont et al. 2014; van Kempen et al. 2014). While 3C84 shows significant long-term time variability, the ALMA 3 mm data show it is stable to within ∼5% (peak to peak) in the two months leading up to and encompassing our MUSTANG-2 observations. We assume an interpolated flux density of 23.8 Jy at 3.3 mm based on the ALMA 91.5 GHz measurements.

The telescope beam was mapped using both 3C84 and the secondary calibration source, J0530+135. The main beam has an FWHM between 9.″1 and 9.″6, varying with time depending on the thermal state of the antenna. Beam size variations larger than this are removed by periodic "Out of Focus Holography" measurements (Nikolic et al. 2007). An error beam is evident with a peak normalization ∼4% of the main beam and a FWHM ∼30″. The ratio of main beam area to error beam area is seen to be 2.42 in the stacked beam maps from 0530+135, and 2.35 in the beam maps using 3C84. The characteristics of the beam determined from individual, quick maps of these sources are consistent with the beam characteristics determined from stacked measurements, indicating that telescope pointing has been well corrected in the maps.

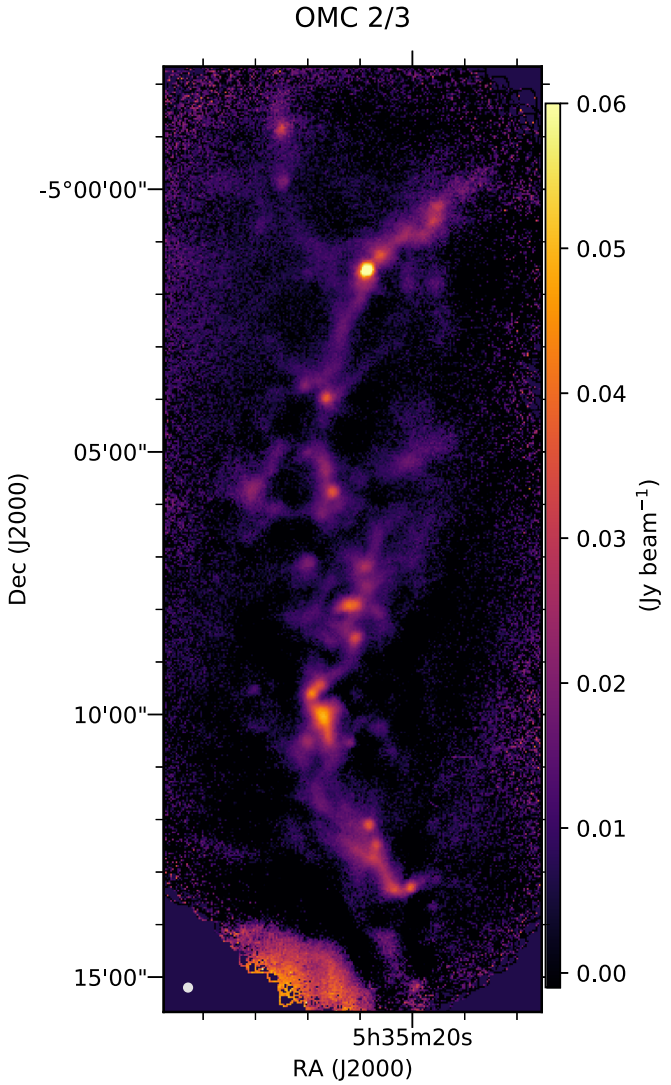

Figure 1. The 3.3 mm MUSTANG-2 map at full angular resolution. The H II region M43 can be seen toward the lower edge of the map. The 9″ MUSTANG-2 beam is depicted in gray in the lower left corner.

Figure 1 shows the MUSTANG-2 map of OMC 2/3. The shape and intensity of the features seen in this map correspond very well with those in the MUSTANG-1 map presented in S14. Despite being made in a much shorter time (40 minutes on source versus 14 hr on source) the new map has slightly lower noise than the old map (0.8 mJy bm^{-1} versus 1.0 mJy bm^{-1}). Due to the larger FOV (4.′25 versus 42″), MUSTANG-2 data allow the large-scale features to be reconstructed more easily, whereas S14 needed to use a more complex, iterative imaging algorithm to do so. This comes about because an important step in imaging ground-based, millimeter continuum cameras is removing atmospheric emission. Generally, this has the effect of filtering out spatial scales larger than the camera's instantaneous FOV. S14 present details on the approach used to reconstruct larger scales from the original MUSTANG observation, and Romero et al. (2019) present a quantitative evaluation of the transfer function of the IDL analysis pipeline used in this work.

We performed a quantitative comparison between the maps by gridding them on the same set of pixels, and placed them on a common surface brightness scale by correcting for the modest difference in beam size between the images, which arises from the differing aperture illumination patterns of MUSTANG and MUSTANG-2. Selecting all (3557) pixels that are above 3σ in both maps, we find a median ratio of old to new pixel values of 0.95 and a mean ratio of 1.0. A least-squares fit for the slope old pixel values as a function of new pixel values yields a slope of 1.03. The 3 mm maps of OMC 2/3 are thus robustly in agreement in spite of having been made with a different instrument, as well as different calibrations and image reconstruction techniques.

An H II region is visible at the southern edge of the MUSTANG-2 map. This H II region, M43, is generated by the early B-star HD 37061/Nu Ori (Simón-Díaz et al. 2011). It is also evident in the GISMO (2.1 mm) map (S16) and as a cavity at 850 μm from SCUBA-2 (Salji et al. 2015). Inspection of these maps along with the 21 cm continuum image (NVSS, Condon et al. 1998) reveals that the 3 and 2 mm maps, while probably dominated by free–free emission toward the H II region, have features that are not seen at 21 cm. This suggests some amount of dust contamination, a conclusion supported by measurements in the far-IR (Smith et al. 1987). These features are particularly noticable at the outer edge of M43.

The MUSTANG-2 map of OMC-2/3 is publicly available on the Harvard Dataverse (doi:10.7910/DVN/EWN4RK).

2.2. GBT 1 cm Observations

After confirming the enhanced 3 mm emission originally seen with MUSTANG, the MUSTANG-2 team obtained Director's Discretionary Time on the GBT at the *Ka* band (program code AGBT18A-446). The observations used the Caltech Continuum Backend to perform sensitive, wide-band continuum beam switching, and the data were calibrated and reduced using the standard procedures described in Mason et al. (2009). These observations, unlike the others reported here, consist of single-pointing photometric measurements targeting selected regions. Each measurement also has two "off" or reference positions offset in azimuth that are generated by the combination of electronic beam switching and telescope nodding, as described in Mason et al. (2009). Photometric data were collected targeting the location with the highest 3 mm brightness in each of the 24 regions or "slices" studied in detail (see Section 3.1) on 2018 March 5. The data were calibrated with respect to 3C138, using VLA *Ka*-band data obtained on 2018 February 26 as part of VLA polarization calibration (service mode) observations. The VLA observations of 3C138, calibrated relative to 3C286 using the standard VLA calibration scale, indicate a flux density of 0.86 Jy for 3C138. While the GBT *Ka*-band receiver provides four separate, 3.5 GHz channels covering the 26-40 GHz receiver band, the four channels have been averaged for the purposes of this analysis in order to avoid overweighting the 1 cm spectral information.

Astronomical signal in the reference positions will generate a negative offset in the photometric measurement. Only one measurement—that of Slice 2—was clearly affected by contamination in the reference position. While we cannot rule out low-level contamination in other positions, the reference positions were separated from the on-source positions primarily in R.A., i.e., off the filament. Furthermore, the 78″ separation between the main position and each of the reference positions is comparable to the typical 1′–1.′5 half-lengths of the slices used to extract photometry at shorter wavelengths (Section 3.1), such that all the points in a given SED should have comparable reference levels. Significant emission was clearly detected in all but one of the 24 pointing positions. The exception is the previously mentioned Slice 2, which has been excluded from all further analysis.

Table 1
Positions, Flux Densities, and Free–Free Corrections (ff_{corr}), if applicable, for the GBT 1 cm Measurements of 24 Regions in OMC 2/3

Slice	R.A. (J2000)	Decl. (J2000)	S_{31} (mJy bm^{-1})	ff_{corr} (mJy bm^{-1})
1	$05^h35^m30^s$	−04°58′49″	1.32 ± 0.12	···
2	$05^h35^m28^s$	−04°59′44″	−0.64 ± 0.11	···
3	$05^h35^m14^s$	−04°59′32″	1.31 ± 0.12	···
4	$05^h35^m18^s$	−05°00′22″	3.01 ± 0.12	0.10
5	$05^h35^m19^s$	−05°00′43″	2.56 ± 0.12	···
6/7	$05^h35^m23^s$	−05°01′33″	6.11 ± 0.12	0.12
8	$05^h35^m25^s$	−05°02′31″	1.25 ± 0.12	···
9	$05^h35^m26^s$	−05°03′07″	0.38 ± 0.12	···
10	$05^h35^m26^s$	−05°03′55″	2.02 ± 0.12	0.5
11	$05^h35^m19^s$	−05°05′11″	2.11 ± 0.12	···
12	$05^h35^m26^s$	−05°05′43″	1.45 ± 0.12	0.7
13	$05^h35^m17^s$	−05°06′03″	1.21 ± 0.12	···
14	$05^h35^m24^s$	−05°07′01″	1.91 ± 0.12	1.0
15	$05^h35^m25^s$	−05°07′56″	2.70 ± 0.12	0.24
16	$05^h35^m35^s$	−05°08′21″	0.52 ± 0.12	···
17	$05^h35^m26^s$	−05°09′02″	1.27 ± 0.16	···
18	$05^h35^m27^s$	−05°09′33″	5.00 ± 0.16	1.7
19	$05^h35^m27^s$	−05°09′56″	5.34 ± 0.16	0.7
20	$05^h35^m26^s$	−05°10′57″	0.66 ± 0.16	···
21	$05^h35^m26^s$	−05°11′32″	1.34 ± 0.16	···
22	$05^h35^m23^s$	−05°12′07″	3.28 ± 0.16	···
23	$05^h35^m23^s$	−05°12′38″	1.46 ± 0.16	···
24	$05^h35^m20^s$	−05°13′19″	1.70 ± 0.16	···

Note. Note that Slice 2 was not used in the analysis and interpretation due to contamination in one of the beamswitch reference positions.

There are a number of very young stellar systems in OMC 2/3 that can give rise to thermal bremmstrahlung emission. Reipurth et al. (1999, hereafter R99) mapped this region at 8″ resolution using the VLA at 8.3 GHz and detected 14 sources. We have used this source list, converted into a map, assuming an optically thin free–free spectrum ($\propto\nu^{-0.1}$), and smoothing to the 24″ GBT 1 cm resolution, to correct the GBT data for free–free emission. Eight regions had non-zero corrections. Of these, the corrections to the measured flux densities of four regions were >15%: slice 10 (25%), slice 12 (48%), slice 14 (52%), and slice 18 (34%). The *Ka*-band measurements and their free–free corrections are summarized in Table 1.

2.3. Archival Data

In order to interpret these data we bring to bear the 1.2 mm MAMBO map presented in S14 along with the multi-wavelength data set presented by S16: 2 mm data from GISMO on the IRAM 30 m; 450 and 850 μm SCUBA-2 maps from the JCMT Gould Belt Survey (Mairs et al. 2016); and *Herschel* 160 μm–350 μm maps (Stutz & Kainulainen 2015). These data sets, convolved to a 25″ (FWHM) common resolution, are shown in Figure 2. *Herschel* 500 μm data were not used

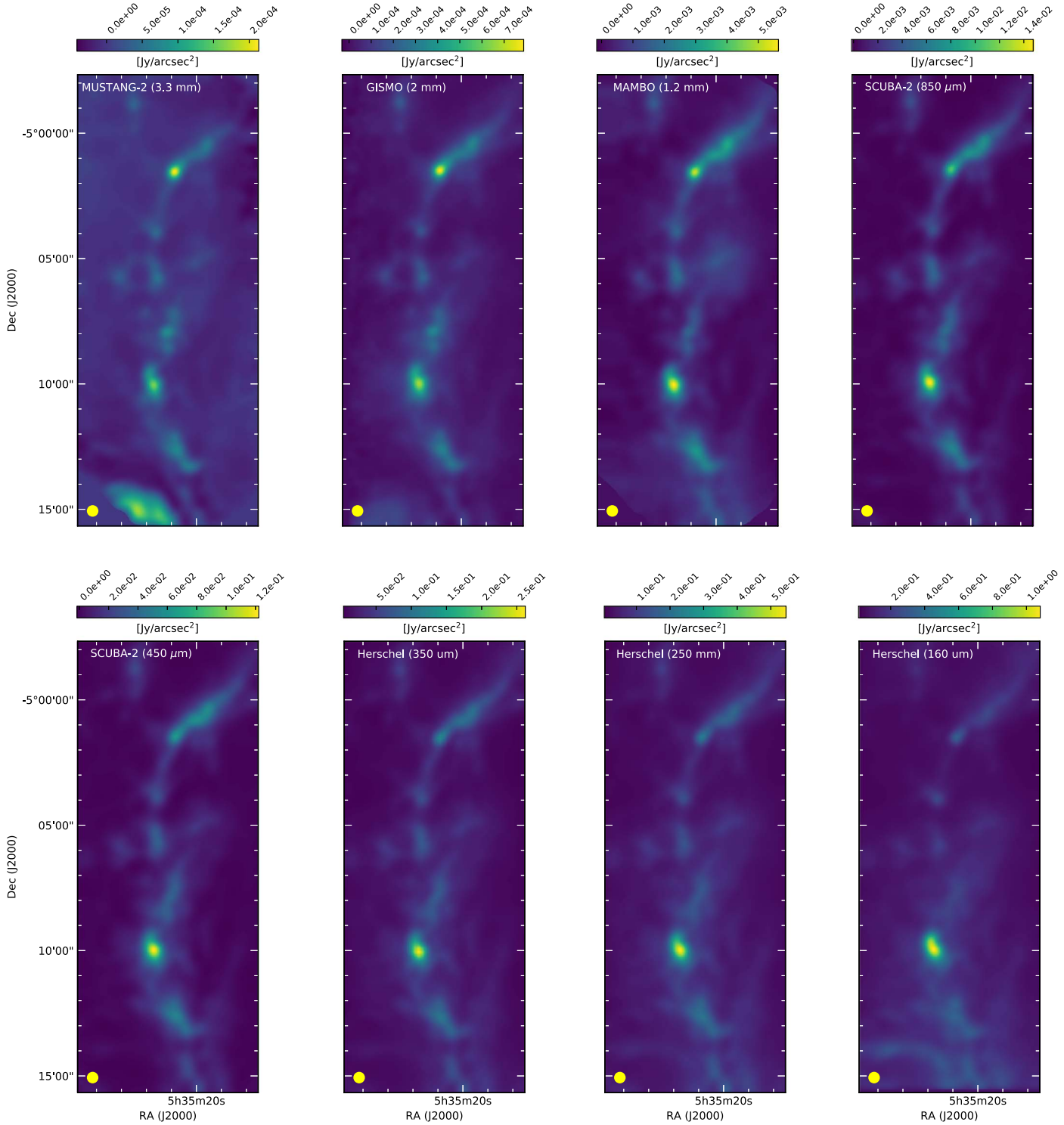

Figure 2. MUSTANG-2, GISMO, MAMBO, SCUBA-2, and *Herschel* maps used in this analysis. All maps have been smoothed to 25″, which is the native resolution of the *Herschel* 350 μm map.

because they were very close in wavelength to the SCUBA-2 450 μm data but had worse angular resolution.

OMC 2/3 has also been observed by ALMA at a similar frequency range to the observations we report here under the auspices of project `2013.1.00662.S` (PI: D. Mardones). These data covered OMC-2 and OMC-3 over a narrow (91.2–91.7 GHz) frequency range at a spectral resolution of ∼35 kHz with the ALMA Compact Array (ACA). The ACA data have similar angular resolution as the MUSTANG-2 data we present here, but the nature of interferometry limits the scales recovered to <90″ for the given projected antenna spacing in the 7 m array (the so-called "missing flux problem"). This is sufficient to compare the flux densities of the more or less discrete sources seen in the 3 mm continuum maps, and to search for line contamination of the MUSTANG-2 data (Section 4.1). The continuum fluxes are consistent to within a few percent.

2.4. Instrumental Bandpasses

With the exception of the *Herschel* data, all of the data products used in this analysis are calibrated such that the flux densities represent response-weighted average values $\langle S \rangle$ across the instrument bandpass,

$$\langle S \rangle \equiv \frac{\int d\nu\, S(\nu)\, R(\nu)}{\int d\nu\, R(\nu)},$$

where $S(\nu)$ is the flux density of the target as a function of frequency and $R(\nu)$ is the spectral response of the instrument. The quantity $\langle S \rangle$ is proportional to integrated power, and it is effectively the quantity that results from calibrating the data into units of power.

To facilitate modeling and interpretation, a spectral response curve $R(\nu)$ was downloaded for each instrument and its corresponding response-weighted center frequency was calculated

$$\nu_0 = \frac{\int d\nu\, \nu\, R(\nu)}{\int d\nu\, R(\nu)}. \quad (2)$$

To calculate the GBT telescope efficiency as a function of frequency a 240 μm (rms) surface was assumed (Hunter et al. 2011; Frayer et al. 2019). These response-weighted frequencies, shown in Table 2, are used in evaluating spectral models (Section 3.2). Compared to using nominal bandpass centers as representative frequencies, adopting these response-weighted frequencies will minimize differences between monochromatic flux densities and band-averaged flux densities. Section 3.2.3 presents a quantitative evaluation of the remaining effect. Table 2 also presents the effective bandwidth for each instrument, which we define as

$$\Delta\nu_{\rm eff} = \frac{\left(\int d\nu\, R(\nu)\right)^2}{\int d\nu\, R^2(\nu)}. \quad (3)$$

Herschel data are pipeline-calibrated to equivalent monochromatic flux densities assuming a fiducial ν^{-1} spectrum. We convert these standard monochromatic flux densities S_s (ν_s) into band-averaged flux densities $\langle S \rangle$ using the relationship provided in the *Herschel* documentation[8]

$$\langle S \rangle = S_s(\nu_s) \times \frac{\int d\nu\, (\nu_s/\nu)\, R(\nu)}{\int d\nu\, R(\nu)}, \quad (4)$$

where ν_s is a chosen reference frequency, not in general equal to the response-weighted frequency given by Equation (2). For *Herschel* the reference frequencies are those which correspond to $\lambda = 350$, 250, and 160 μm. These $\sim$1% corrections were applied, resulting in band-averaged flux densities.

[8] The SPIRE Handbook (HERSCHEL-HSC-DOC-0798, version 3.2, 2018 December 19) and the PACS Explanatory Supplement (HERSCHEL-HSC-DOC-2101, version 4.0.1, 2019 April 30).

Table 2
Response-weighted Average Frequencies and Effective Bandwidths for Each Instrument in This Analysis

Instrument	ν_o (GHz)	$\Delta\nu_{\rm eff}$
GBT (1cm)	33.0	14
GBT (MUSTANG-2)	87.7	28
GISMO	150.6	29
MAMBO	254.9	132
SCUBA-2 (850 μm)	354.0	45
SCUBA-2 (450 μm)	668.1	67
Herschel (350 μm)	871.9	296
Herschel (250 μm)	1221.8	420
Herschel (160 μm)	1910.7	975

3. Analysis

3.1. SED Extraction

We used the matched 25″ resolution, multi-wavelength maps shown in Figure 2 to construct SEDs for a set of regions along the OMC 2/3 filament. Accurately extracting information from astronomical images made at different wavelengths, and with different telescopes and different data reduction algorithms, can be difficult due to the different systematics in the images. In order to cleanly focus on the spectrum of specific structures in the maps, and to better account for variable local backgrounds and zero levels in the maps, we have undertaken an analysis in which we define a set of 24 lines or "slices" across structures of interest in the maps. The locations of these slices are shown in Figure 3; these slices were also used to define the pointings for the 31 GHz photometry described in Section 2.2. In addition this figure shows the locations of protostars, starless cores, and free–free emission from young stellar objects (Reipurth et al. 1999; Sadavoy et al. 2010). The surface brightness profile of each map along each slice is extracted, and we remove a mean and slope from each profile at each wavelength. The mean and slope are measured from the first and last 2% of pixels along the slice. When we follow this procedure we find that the resulting profiles, when renormalized to the peak intensity, track each other remarkably well: the rms of the individual-wavelength profiles about the mean normalized profile is 9% on average, with a highest dispersion of 15% (Slice 10) and a lowest dispersion of 5% (Slice 6). This 9% rms scatter between the individual-wavelength profiles about their average is indicative of the maximum extent to which differences in the spatial filtering implicit in the maps is affecting the SEDs of the structures we are examining; it is an upper limit because astrophysical variations will also give rise to variations between the slice profiles at different wavelengths. We take the peak value of the sky brightness across a slice to be the value of the SEDs at that wavelength; in this manner the SED of the filament or object at the center of each slice is assembled, from 3 mm (MUSTANG-2) to 160 μm (*Herschel*). The 1 cm SED points are determined from the pointed GBT nod observations, renormalized to the same surface brightness units. Calibration uncertainties dominate the spectral analysis: we assume a 10% calibration uncertainty associated with each SED point. For the 1 cm data the measurement error is added in quadrature.

The SEDs for the 24 regions of OMC 2/3 studied here are shown in Figure 4–7. In general, and as discussed in Section 3.2, the $\lambda > 2$ mm data are seen to be higher than

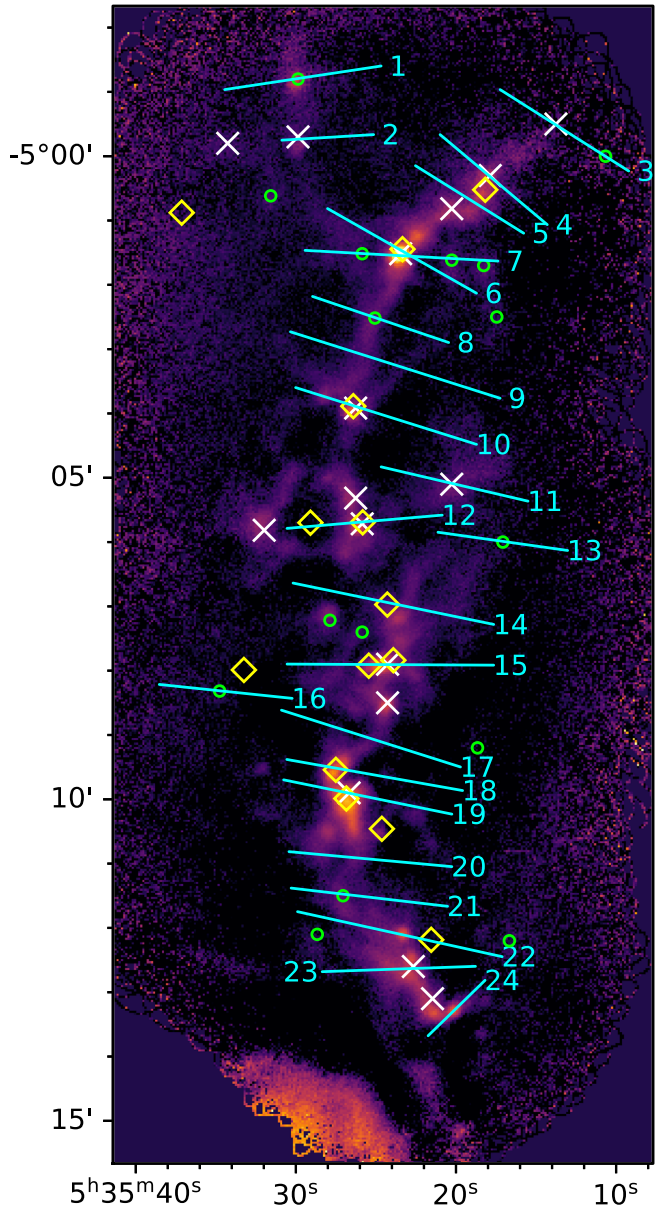

Figure 3. MUSTANG-2 map, with the 24 "slices" developed for detailed SED analysis shown in cyan. Green circles mark the locations of known starless cores in the field (Sadavoy et al. 2010); yellow diamonds mark the locations where likely free–free emission has been identified from 8.3 GHz VLA observations of R99; and white X's mark the locations of protostellar cores (Sadavoy et al. 2010).

expected based on extrapolations from shorter wavelengths. Salient characteristics of some of the individual regions are as follows.

1. Slice 2: GBT data rejected due to contamination in the reference beam.
2. Slice 6 and 7: redundant measurements of the brightest object in the 3 mm map, MMS6. The peak brightness at 3 mm was 90 mJy per 10″ beam.
3. Slices 11 and 13: the 1 mm data point was anomalously high. Since these are isolated anomalies, and since the 1 mm map is clearly discrepant with the morphologies evident at other wavelengths in this region, the 1 mm data points were excluded from analysis.

3.2. Modeling

The MBB is the spectrum generated by optically thin thermal radiation from dust grains at a temperature $T_{\rm d}$ and having a power-law opacity proportional to ν^{β}:

$$I(\nu) \propto \frac{\nu^{(3+\beta)}}{\exp(h\nu/kT_{\rm d}) - 1}. \quad (5)$$

Given the elevated long-wavelength emission we seek to quantify, we have studied two different selections of our data with two different variants of the MBB. The four cases are as follows:

1. MBB2mm: we fit the $\lambda \leqslant 2$ mm data to a standard MBB.
2. MBB2mm_ext: uses the models resulting from MBB2mm, but evaluating goodness of fit with respect to the entire SED, i.e., the fits are extrapolated to longer wavelength.
3. MBBall: all SED points for a given target are jointly fit to a single MBB.
4. MBBall_2beta: same as MBBall, but a spectral break is introduced at 120 GHz with an independent emissivity index β' to model long-wavelength emission.

The χ^2 per degree of freedom and number of degrees of freedom n for each of these analyses are given in Table 3, and each analysis is discussed in more detail in the following sections. For the purposes of fitting and evaluating χ^2, the MBB is evaluated at each instrument's response-weighted frequency ν_0 (Section 2.4). The effect of residual band-averaging effects (or color corrections) on the model predictions is quantified in Section 3.2.3.

3.2.1. Fitting $\lambda \leqslant 2$ mm (MBB2mm, MBB2mm_ext)

We first attempt a standard MBB fit, as done before for very similar data in S16. This is the analysis we call MBB2mm, and we find it gives reasonable fits to the 2 mm and shorter-wavelength data, with a median over the 24 "slices" of $\chi^2_n = \chi^2/n = 1.65$ for $n = 4$ degrees of freedom, a minimum $\chi^2_n = 0.11$ and a maximum $\chi^2_n = 9.11$.

When we extrapolate these fits to the entire measured SED, however, we find considerably poorer consistency. This is the case we call MBB2mm_ext. It has a median χ^2_n of 9.48 for $n = 6$ degrees of freedom, a minimum $\chi^2_n = 3.09$ and a maximum $\chi^2_n = 22.26$. The poor fits are due to the 3 mm and 1 cm data points systematically lying above the extrapolated fits to the short-wavelength data: 23 of 24 3 mm SED points lie above the short-wavelength MBB fit, with a median excess of 5.0σ; 22 of these 23 have a 3σ or greater excess. Similarly, 22 of 23 of the 1 cm data points lie above the extrapolated MBB, also with a typical magnitude of 5.0σ, and the single point below the fit is not statistically significant (0.1σ). The average residual brightness is $(1.96 \pm 0.35) \times 10^{-6}$ Jy arcsec^{-2} at 1 cm and $(3.28 \pm 0.64) \times 10^{-5}$ Jy arcsec^{-2} at 3.3 mm. In fractional terms the 1 cm data points themselves are 5.19 ± 1.03 times as bright as the extrapolated MBB, and the 3.3 mm data are 2.01 ± 0.15 times as bright as the model extrapolation.

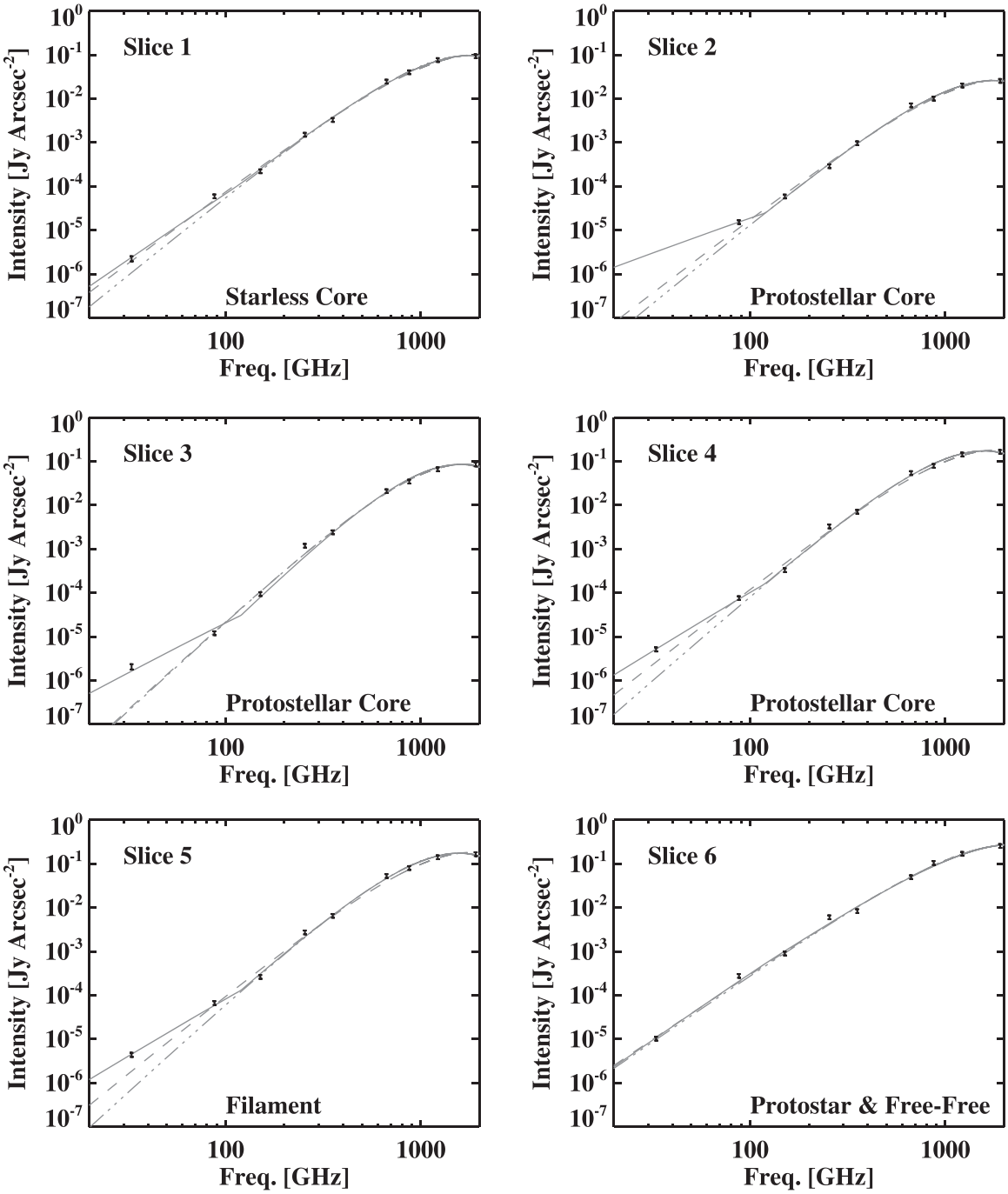

Figure 4. SED for slices 1–6. The solid line is the broken modified blackbody fit to the data; the dashed line is a standard modified blackbody fit to the data; and the dashed–dashed–dotted line is a standard modified blackbody fit to the $\lambda \leqslant 2$ mm data only.

3.2.2. Fitting All the Data (MBBall, MBBall_2beta)

Including the long-wavelength points in the MBB fit still yields poor χ^2_n values, with a median $\chi^2_n = 5.23$ (minimum = 2.76, maximum = 17.44) for $n = 6$ and the long-wavelength data systematically above the model. This is the case we call MBBall. In this case 19 of 23 1 cm SED points lie above the fit (typical SNR = 1.9σ) and 23 of 24 3 mm SED points lie above the fit (typical SNR 2.7σ).

To better accommodate the long-wavelength data we allow a different power-law β' at $\nu < 120$ GHz ($\lambda > 2.5$ mm; we refer to this case as MBBall_2beta. The break frequency was chosen to lie midway between the GISMO and MUSTANG-2 bandpass centers. For a discussion of a physical motivation of this generalization, see Section 4.4. We find a considerably improved fit, with a median $\chi^2_n = 2.98$ for $n = 5$ (minimum = 0.84, maximum = 7.79). The residuals to the MBBall_2beta fit still show systematic trends, with 22 of the 23 1 cm SED points falling *below* the fit and 23 of the 24 3 mm SED points still falling above it. This suggests that the spectral shape at $\lambda > 2$ mm may not be well-represented by a pure, single power law. This fact is also reflected in the lower χ^2_n for the single blackbody fit to the short-wavelength data (MBB2mm: 1.65) compared to the double-beta blackbody fit to *all* the data (MBBall_2beta: 2.98). The limited spectral

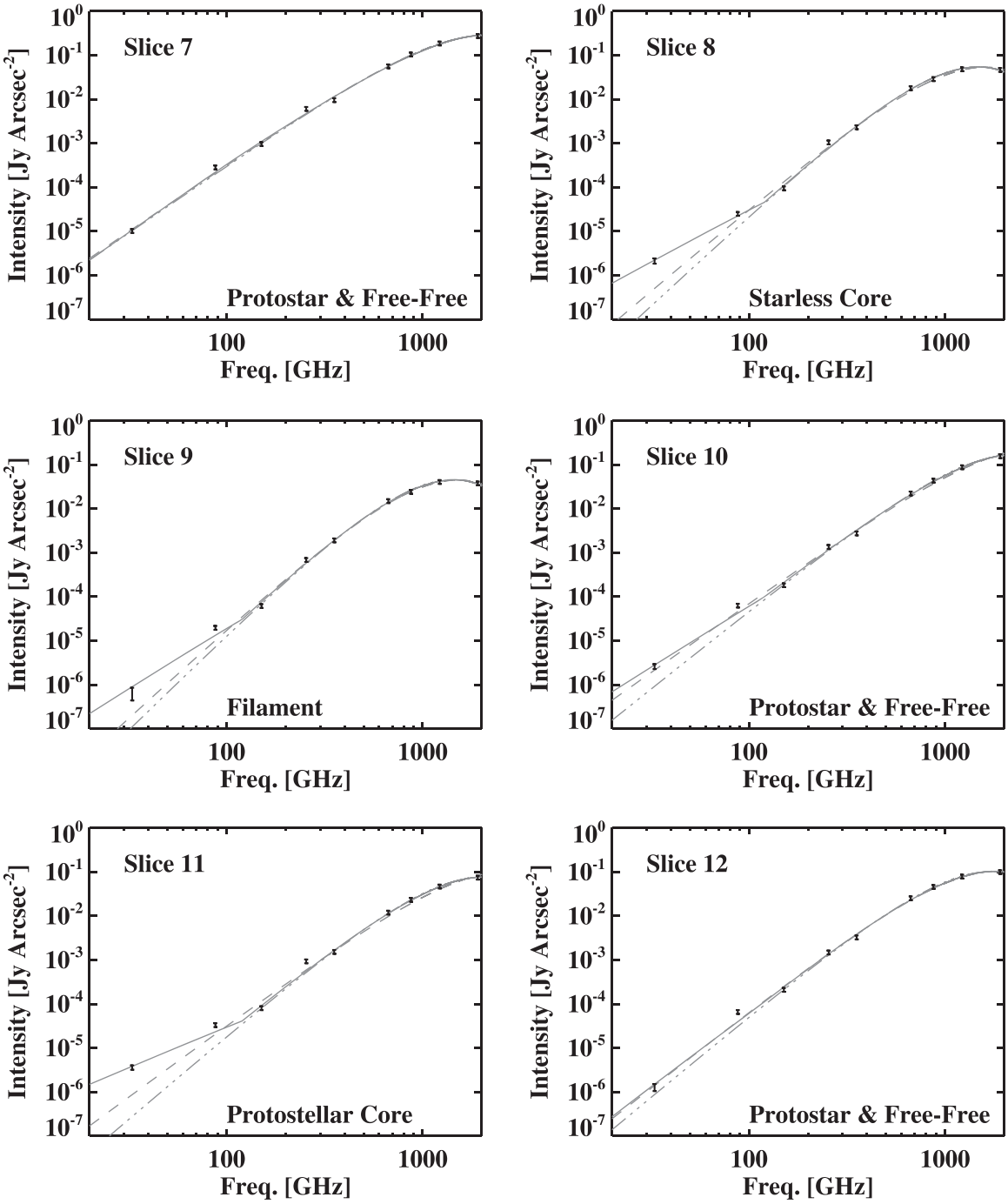

Figure 5. SED for slices 7–12. Lines are the same as those in Figure 4.

coverage of our data set in this regime, however, would not support introducing more parameters into the analysis, and no single, plausible physical model provides a better description of the long-wavelength residuals (Section 4). Nevertheless, of the models we considered the double-beta MBB model clearly provides the best description of the data set as a whole.

Table 3 shows χ^2_n and n values for all four of the modeling approaches described above. The χ^2_n of MBBall_2beta is lower than that in the MBBall analysis for 19 of 24 regions. The statistical significance of the reduction in χ^2 achieved by allowing an extra parameter (β') to be free in the model fit can be evaluated by the F-test. The F statistic is computed as

$$F = \frac{\Delta\chi^2}{\chi^2_{n,u}}, \tag{6}$$

where $\Delta\chi^2$ is the change in χ^2, which has resulted from adding the additional parameter(s), and $\chi^2_{n,u}$ is the reduced χ^2 for the "unrestricted" model fit, in this case, the one which also allows β' to be a free parameter. For eight individual regions the reduction in χ^2_n is significant at the 95% level by this test; these regions are indicated by bold entries in Table 3. The physical environments of these eight regions are varied: three are

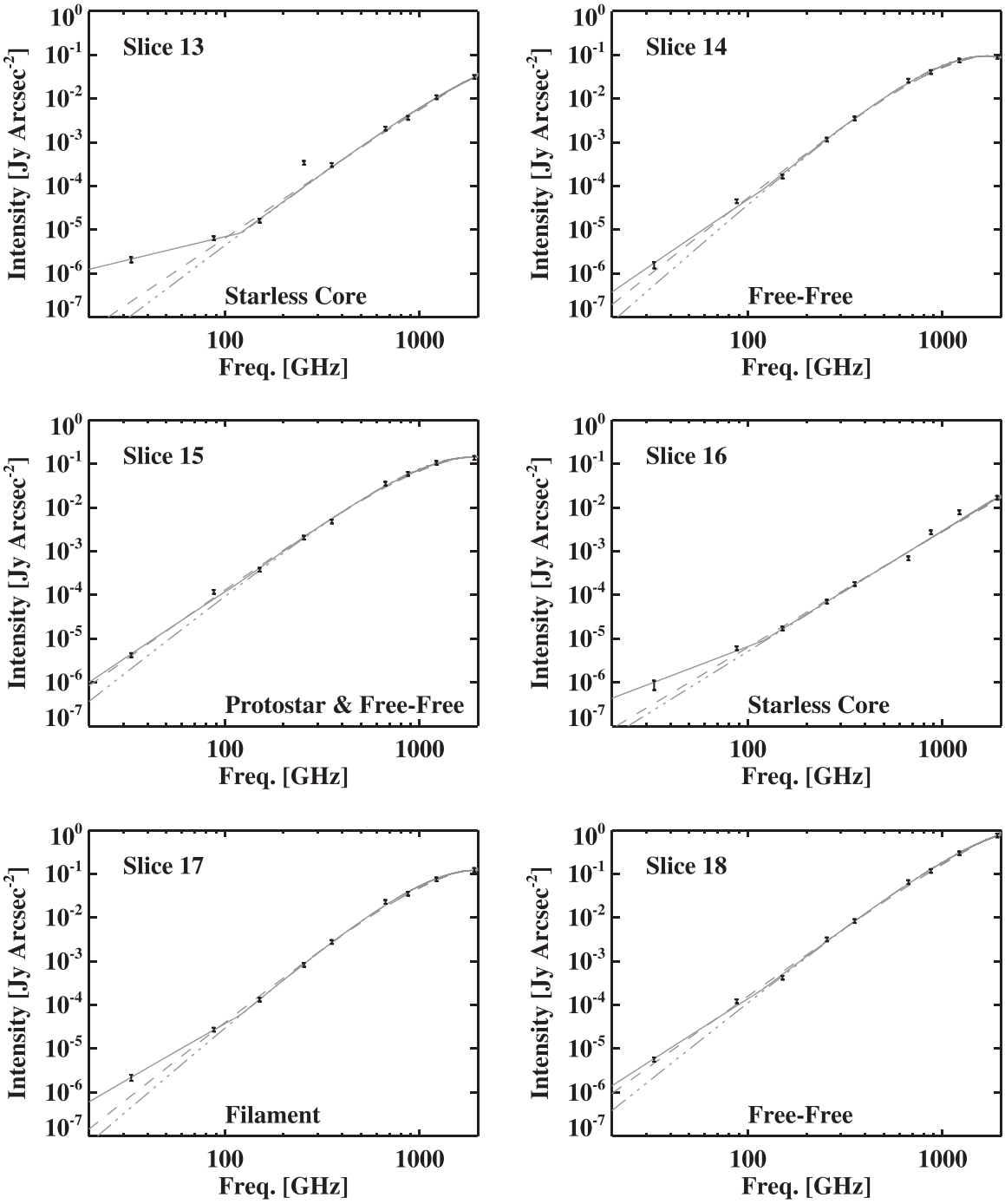

Figure 6. SED for slices 13–18. Lines are the same as those in Figure 4.

starless cores, two are protostellar cores, one has a known free–free source, and two sample filamentary dust emission. In no case is the simple MBB significantly preferred over MBBall_2beta.

Table 4 shows the fitted parameter values from the MBBall_2beta analysis for each region studied, and Table 5 summarizes the typical parameters for each of the types of objects we studied. The values of β and $T_{\rm d}$ obtained are generally consistent with those obtained in this region by measurements of ammonia transitions (Friesen et al. 2017), as well as by the similar millimeter/submillimeter continuum study of this region by S16. The dust temperatures are coldest (15.2 ± 0.5 K) in the filament, and progressively warmer in starless cores, cores with protostars, and finally warmest in regions with detected free–free sources (20.4 ± 0.6 K). The long-wavelength β' averages 0.74 ± 0.03, though it is strikingly flatter for starless cores than in other regions ($\beta' = 0.21 \pm 0.06$).

3.2.3. Effect of Color Corrections

The models described in the previous sections are evaluated at the response-weighted center frequency of each instrument's bandpass, as described in Section 2.4. This is equivalent to approximating the spectrum as a mean plus a slope across the

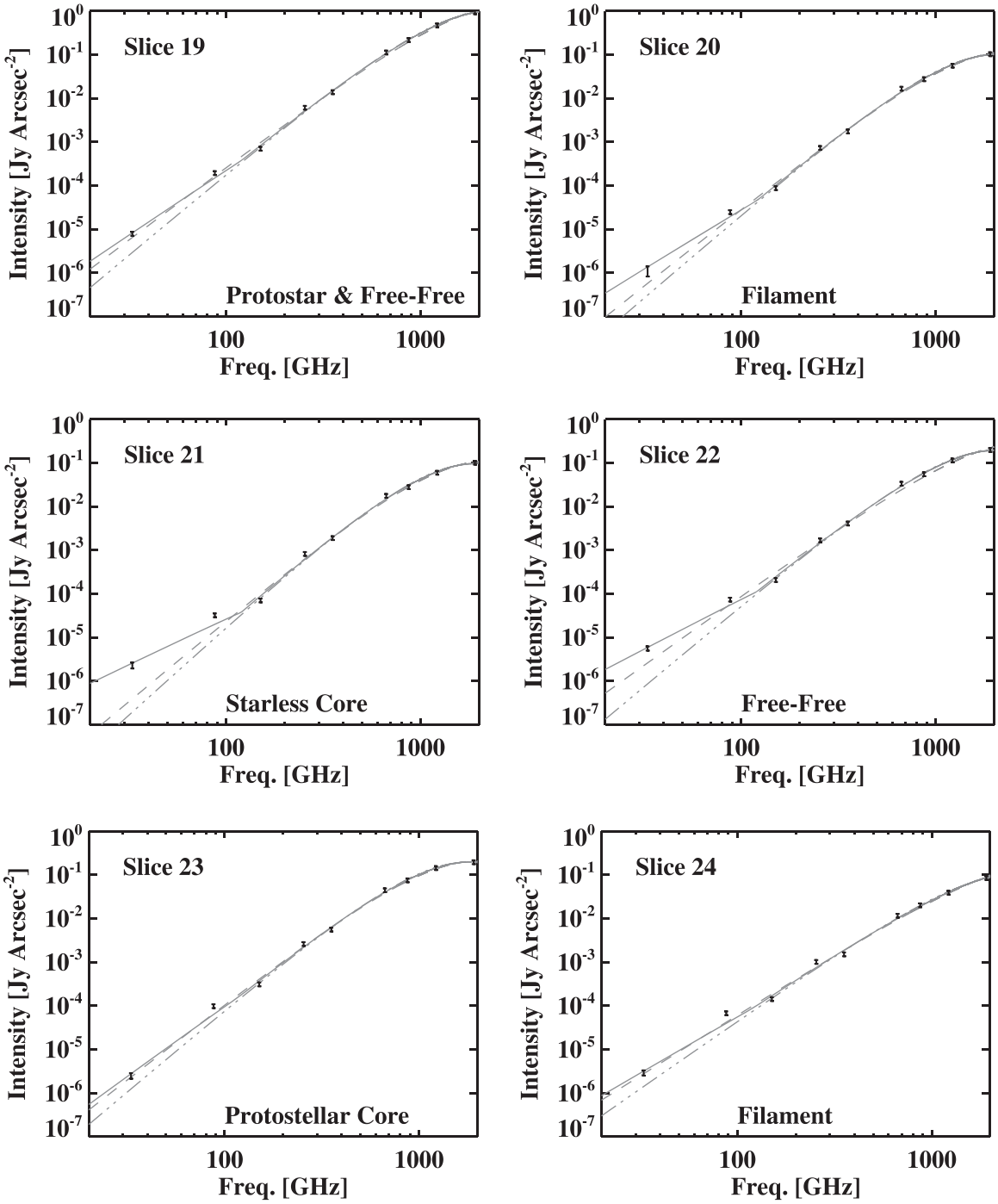

Figure 7. SED for slices 19–24. Lines are the same as those in Figure 4.

bandpass. To test the validity of this approximation we computed multiplicative corrections to the model spectrum values:

$$C_{i,j} = \frac{\langle M_i(\nu)\rangle_j}{M_i(\nu_{0,j})}$$

where M_i is the MBBall_2beta best-fit model for region i, $\nu_{0,j}$ are the response-weighted frequencies for the band in question, and the averages are over the j bandpasses. For the spectral average the applicable instrument bandpass is used. In effect these corrections convert the (approximate) monochromatic model predictions into bandpass-averaged model predictions, a conversion that is exact if the spectrum assumed to calculate $C_{i,j}$ is correct. The largest corrections are for MAMBO (mean and rms over regions: 1.08 ± 0.02), HERSCHEL-PACS 160 μm (0.97 ± 0.02), and GBT 1 cm (1.03 ± 0.02). These three instruments have the largest fractional bandwidths in our analysis, with $\Delta\nu_{\rm eff}/\nu_0 \sim 40\%$–$50\%$. The MBBall_2beta fit was then repeated with the color-correction factors applied to the model predictions. The typical (median over regions) impact of the color correction on β is 0.3σ while for β' it is 0.1σ, with the largest differences being 1.0σ and 0.7σ,

Table 3

$\chi^2_n = \chi^2/n$ for the Four Fits Described in the Text (Section 3): The Short-wavelength MBB fit (MBB2mm); the Short-wavelength MBB Fit Evaluated Relative to All Data (MBB2mm_ext); the MBB Fit to All Data (MBBall); and a "Broken Modified Blackbody" Fit to All Data (MBBall_2beta)

	χ^2/n (n)			
Slice	MBB2mm ($\lambda \leqslant 2$ mm)	MBB2mm_ext (All Data, extrap.)	MBBall (All Data, fit)	MBBall_2beta (All Data)
1	1.12 (4)	6.24 (6)	2.76 (6)	2.27 (5)
2	1.50 (4)	5.53 (5)	3.84 (5)	1.50 (4)
3	3.90 (4)	9.48 (6)	9.44 (6)	7.20 (5)
4	2.89 (4)	12.80 (6)	8.22 (6)	**2.39** (5)
5	2.48 (4)	14.97 (6)	10.29 (6)	**2.39** (5)
6	4.20 (4)	4.68 (6)	4.25 (6)	4.94 (5)
7	2.42 (4)	3.09 (6)	2.91 (6)	3.28 (5)
8	2.51 (4)	12.99 (6)	10.26 (6)	**2.31** (5)
9	1.68 (4)	8.93 (6)	7.33 (6)	4.20 (5)
10	1.61 (4)	10.41 (6)	5.23 (6)	4.00 (5)
11	0.11 (3)	22.26 (5)	17.44 (5)	**2.98** (4)
12	1.13 (4)	5.98 (6)	4.08 (6)	4.79 (5)
13	1.52 (3)	16.64 (5)	13.89 (5)	**1.31** (4)
14	0.50 (4)	7.15 (6)	3.85 (6)	2.23 (5)
15	0.81 (4)	8.19 (6)	3.21 (6)	3.20 (5)
16	9.11 (4)	10.44 (6)	9.25 (6)	7.79 (5)
17	1.03 (4)	6.75 (6)	4.60 (6)	**0.84** (5)
18	1.10 (4)	8.69 (6)	3.66 (6)	2.09 (5)
19	1.46 (4)	10.22 (6)	4.35 (6)	2.53 (5)
20	1.72 (4)	6.57 (6)	4.59 (6)	2.73 (5)
21	3.65 (4)	16.54 (6)	14.63 (6)	**6.41** (5)
22	1.41 (4)	16.09 (6)	10.75 (6)	**2.76** (5)
23	1.65 (4)	7.68 (6)	4.43 (6)	4.48 (5)
24	3.81 (4)	10.39 (6)	6.58 (6)	7.15 (5)
Median	1.65	9.48	5.23	2.98
Min.	0.11	3.09	2.76	0.84
Max.	9.11	22.26	17.44	7.79

Note. The number of degrees of freedom n is given for each in parentheses. The eight regions for which the broken blackbody fit (MBBall_2beta) has a χ^2_n lower than the all-data MBB χ^2_n at 95% confidence are indicated by bold values in the last column.

respectively. There is a modest shift in the median T_d of -0.3σ, with the largest shift for an individual region being -0.8σ.

4. Interpretation

Our results indicate that a single MBB SED provides a considerably better description of the 2 mm to 350 μm SED than it does when the GBT 3.3 mm and 1 cm data are included ($\chi^2_n = 1.65$ for $\lambda \leqslant 2$ mm versus $\chi^2_n = 5.23$ when-long-wavelength data are included). Similar results were obtained by S16. Structures at 3 mm and 1 cm are seen to be significantly brighter than what would be expected by extrapolating the short-wavelength MBB SED; and the overall SEDs are better described by a "broken" blackbody with a different dust opacity index β' at $\nu < 120$ GHz, than they are a standard single-β MBB (typical $\chi^2_n = 2.98$ versus 5.23). The long-wavelength residuals to a standard MBB fit to the $\lambda < 3$ mm data are shown in Figure 8. As noted in S14, the morphological similarity of the MUSTANG-2 maps with images at shorter wavelengths is a strong indication the 3 mm emission we see is dominated by dust, or by something closely associated with dust in the ISM. In the next three subsections we consider several possible explanations for the observed spectrum of dust-associated emission.

4.1. Spectral Line Contamination

Molecular line emission could in principle contaminate the broadband continuum SEDs we have measured. Transitions of the brightest molecular species in the millimeter regime, CO, lie outside the MUSTANG-2 and GISMO bandpasses. Although CO(2-1) is within the MAMBO bandpass, S14 argue that it is unlikely to significantly contaminate the 1mm continuum measurements. To the extent it does it would tend to steepen 1–3 mm spectra rather than flatten them, and would not contribute to the 1 cm and 3 mm flattening we report.

It is possible that weaker lines could contribute to the measured 3 mm continuum level. Because MUSTANG and MUSTANG-2 have different bandpasses (80–99 GHz versus 75–105 GHz), the excellent agreement between the original MUSTANG maps of S14 and those presented here suggests that that is not the case. To further check this possibility of line contamination we used high spectral-resolution ALMA Compact Array (ACA) data from project `2013.1.00662.S` (Section 2.3) to search for line contamination. These data covered OMC-2 and OMC-3 over a narrow (91.2–91.7 GHz) frequency range at a spectral resolution of $\sim$35 kHz. While several spectral lines are evident (e.g., CH_3CN), their excision changes the integrated continuum fluxes by $<2\%$. Furthermore, the ACA-observed source fluxes agree with the MUSTANG-2 source fluxes within a few percent. We conclude that contamination by spectral lines is unlikely to account for any significant portion of the elevated 3 mm emission we report.

4.2. Free–Free and Synchrotron Emission

Thermal Bremsstrahlung ("free–free") emission is typically the dominant emission mechanism in galaxies in the "trough" between synchrotron and thermal dust emission, 10 GHz to 100 GHz or so. In regions of high-mass star formation, such as OMC 1, thermal free–free is even more prevalent. OMC 2/3 itself does not harbor massive stars or star clusters as does OMC 1, although as previously noted there is an H II region (M43) created by an O/B star immediately to the southeast. Young protostars can give rise to free–free emission, and in fact the 8.3 GHz VLA maps of R99 reveal 14 sources in OMC 2/3 with flux densities between 0.15 mJy and 2.84 mJy. The 8″ beam of these observations is well matched to the scales being studied here, so these data provide a good handle on the contribution of free–free emission to the SEDs of the regions under study. As discussed in Section 2.2, the 31 GHz (1 cm) data reported here have been corrected for free–free using the R99 measurements under the assumption that each source is optically thin at 8.3 GHz. The contribution of optically thin free–free to the 3.3 mm (90 GHz) points is negligible in all regions except one, Slice 14, where it explains $\sim$25% of the peak 3.3 mm surface brightness at the location in question.

While optically thin free–free sources cannot explain any significant portion of the long-wavelength spectral residuals, it is possible that free–free, which is optically thick over at least part of the frequency range measured, could contribute to the observed spectral signal. Such a signal would be spatially unresolved at the resolutions achieved in our data, and have a flux density increasing as ν^2 up to a turnover frequency somewhere between 8.3 GHz (the frequency of the VLA maps in R99) and 100 GHz

Table 4
Fitted Parameter Values

Slice Number	Description	β	β'	T_d
1	Starless Core	1.52 ± 0.10	1.09 ± 0.12	19.44 ± 1.44
2	Protostellar Core	1.67 ± 0.12	−0.32 ± 0.45	18.33 ± 1.39
3	Protostellar Core	2.43 ± 0.10	0.39 ± 0.16	14.04 ± 0.74
4	Protostellar Core	1.89 ± 0.10	0.78 ± 0.11	15.67 ± 0.91
5	Filament	2.03 ± 0.10	0.71 ± 0.11	15.16 ± 0.86
6	Protostellar Core, Free–Free Emission	0.94 ± 0.10	1.09 ± 0.10	28.25 ± 3.31
7	Protostellar Core, Free–Free Emission	0.97 ± 0.10	1.15 ± 0.10	27.09 ± 3.00
8	Starless Core	2.10 ± 0.10	0.47 ± 0.12	14.01 ± 0.71
9	Filament	2.27 ± 0.10	0.86 ± 0.19	13.34 ± 0.65
10	Protostellar Core, Free–Free Emission	1.44 ± 0.10	0.83 ± 0.11	25.88 ± 2.75
11	Protostellar Core	1.68 ± 0.10	−0.09 ± 0.11	21.54 ± 1.83
12	Protostellar Core, Free–Free Emission	1.57 ± 0.10	1.43 ± 0.14	19.19 ± 1.42
13	Starless Core	1.32 ± 0.10	−0.91 ± 0.13	50.34 ± 12.78
14	Free–Free Emission	1.80 ± 0.10	1.10 ± 0.13	17.02 ± 1.10
15	Protostellar Core, Free–Free Emission	1.35 ± 0.10	1.02 ± 0.10	21.31 ± 1.79
16	Starless Core	0.74 ± 0.11	−0.30 ± 0.2	...
17	Filament	1.82 ± 0.10	0.62 ± 0.14	19.76 ± 1.53
18	Free–Free Emission	1.47 ± 0.10	0.89 ± 0.10	34.36 ± 5.31
19	Protostellar Core, Free–Free Emission	1.64 ± 0.10	1.02 ± 0.10	24.78 ± 2.50
20	Filament	1.75 ± 0.10	0.78 ± 0.18	21.59 ± 1.87
21	Starless Core	1.95 ± 0.10	0.17 ± 0.12	19.08 ± 1.43
22	Free–Free Emission	1.65 ± 0.10	0.35 ± 0.10	21.76 ± 1.88
23	Protostellar Core	1.65 ± 0.10	1.27 ± 0.12	19.34 ± 1.44
24	Filament	0.97 ± 0.10	0.61 ± 0.12	39.05 ± 7.18

Note. The dust temperature T_d in region 16 was not usefully constrained.

Table 5
Weighted Average Parameter Values by Physical Characteristics of Target Region; Slice 16 Was Excluded as a Poorly Constrained Outlier

Marker Type	β	β'	T (K)
Filament ($N = 5$)	1.77 ± 0.04	0.69 ± 0.06	15.2 ± 0.5
Starless Core ($N = 5$)	1.55 ± 0.04	0.21 ± 0.06	15.8 ± 0.6
Protostellar Core ($N = 10$)	1.62 ± 0.03	0.86 ± 0.04	17.4 ± 0.4
Free–Free ($N = 8$)	1.48 ± 0.04	0.93 ± 0.04	20.4 ± 0.6
All Regions ($N = 24$)	1.65 ± 0.02	0.74 ± 0.02	16.5 ± 0.3

Note. Error bars represent the error in the mean.

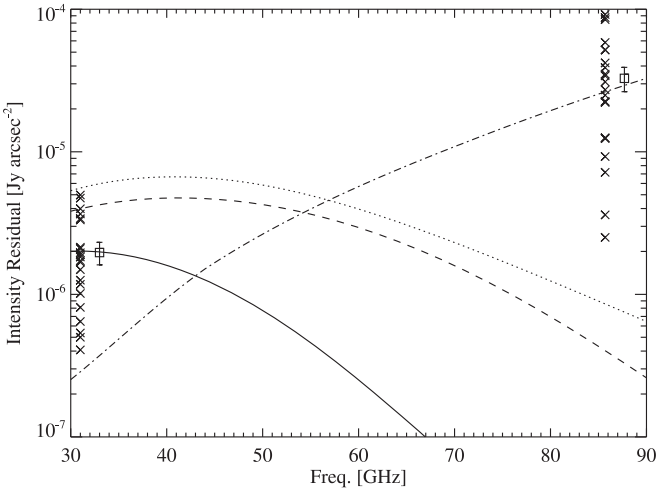

Figure 8. Long-wavelength residuals to the short-wavelength fit (MBB2mm). Square points show the average and error in the mean, with an overall 10% calibration uncertainty added in quadrature. x's slightly offset in frequency are individual slice residuals. Three representative spinning dust spectra are shown for comparison. The solid line is the "Dark Cloud" model; the dashed line is the "Molecular Cloud" model; and the dotted line is the Dark Cloud model with density and temperature values appropriate for OMC 2/3 specifically. The dashed–dotted line shows the spectrum of the $T_d = 17$ K model of Paradis et al. (2011) for dust grain emission including two-level system noise.

or so. In order to account for any significant fraction of the 90 GHz spectral excess the turnover frequency would have to be above 31 GHz in most cases. To test the potential relevance of this mechanism we examined the flux density ratios between 8.3, 31, and 90 GHz for the six regions that have 8.3 GHz free–free sources closely associated with 90 GHz emission. Optically thick free–free with a turnover well above 31 GHz would give $S_{31}/S_{8.3} = (31/8.3)^2 = 13.8$. Five of the six sources with 8.3 GHz detections have $S_{31}/S_{8.3}$ lower than this by a factor of 2–7. The remaining region, slice 15, has $S_{31}/S_{8.3} = 11.25 \pm 0.19$, thus the 90 and 31 GHz measurements could be explained by free–free emission with a turnover between 8.3 and 31 GHz. Were this to be the case, the optically thick free–free still does not contribute significantly to the observed 3 mm spectral residual, since the turnover frequency is too low for it to do so.

Synchrotron radiation does not typically track dust spatially. Dust is prevalent in regions where the ISM is cold, dense, and heavily shielded from ionizing radiation. Synchrotron radiation requires a source of relativistic electrons such as an active galactic nucleus or supernova. If the 31 and 90 GHz signals reported here were generated by diffuse synchrotron or free–free radiation, these structures would be clearly visible in the 8.3 GHz maps of Reipurth et al. (1999) and even more so in the NVSS. This not being the case, synchrotron is clearly not a significant contributor to the SED measurements we report. We can place an upper limit on the surface brightness of synchrotron or free–free radiation using the NVSS, which has

a 45″ (FWHM) beam and a typical sensitivity of 0.45 mJy/bm, or a surface brightness sensitivity of 2.0×10^{-7} Jy arcsec^{-2}. For an optically thin free–free spectrum, this would give a 95% upper limit of 2.8×10^{-7} Jy arcsec^{-2} at 31 GHz and 2.6×10^{-7} Jy arcsec^{-2} at 90 GHz. The corresponding limits on synchrotron are 4.4×10^{-8} Jy arcsec^{-2} (31 GHz) and 2.2×10^{-8} Jy arcsec^{-2} (90 GHz). The limits from Reipurth et al. (1999) are weaker by a factor of ∼3 (free–free) to 8 (synchrotron) due to its lower surface brightness sensitivity and closer proximity in frequency.

4.3. Anomalous Microwave Emission (AME)

High-surface-brightness sensitivity observations in the microwave regime over the past two decades have revealed the widespread presence of dust-associated emission which is not well described by thermal dust emission, thermal bremstrahlung (free–free), or synchrotron radiation (Kogut et al. 1996; de Oliveira-Costa et al. 1997; Leitch et al. 1997). This so-called "AME" is best explained as electric dipole emission from small, charged spinning dust grains (Draine & Lazarian 1998), although there are other plausible models such as magnetic dipole emissions from large, ferrous dust grains (Draine & Lazarian 1999) or spinning nano-silicates (Hoang et al. 2016), and recent observational evidence suggests that nano-diamonds could be relevant in some environments (Greaves et al. 2018). Although most studies of AME target our own Galaxy, it has also been detected in other, nearby galaxies (Murphy et al. 2010, 2018). For a recent review of AME observations and theory see Dickinson et al. (2018).

AME spectra are generally seen to peak in the 20–60 GHz range, with the peak frequency and detailed spectral shape depending on the local physical conditions, including the grain size distribution, the intensity of the radiation field, the dipole moment of the emitting grains, the number density of grains, and the ionization fractions of hydrogen and carbon (Finkbeiner et al. 2004; Planck Collaboration et al. 2011, 2015). We used the SPDUST2 code (Ali-Haïmoud et al. 2009; Silsbee et al. 2011) to compute representative AME spectra. Figure 8 shows spectra for diffuse molecular cloud (MC) and dark cloud (DC) environments, with parameters as in Ali-Haïmoud et al. (2009), as well as the spectrum for a DC environment with density and temperature set to values closer to those observed in the OMC 2/3 filament ($n_H = 10^5$ cm^{-3} and $T_d = 16$ K). For comparison the residuals to the short-wavelength MBB fit (MBB2mm) of the SEDs the 24 individual regions are also shown. The AME models do not match the data well.

It is interesting to note that, as illustrated by Figure 5 of Ysard et al. (2011), standard AME spectra can peak at frequencies as high as 100 GHz or even higher when the interstellar radiation field is strong, $G_0 \gtrsim 5$. While there are several significant sources of ionizing photons nearby—particularly Nu Ori, as well as the Trapezium cluster slightly farther afield—the abundant dust in this very dense MC environment will attenuate these photons over a relatively short distance (although see Jørgensen et al. 2006). When Ysard et al. (2011) compute line-of-sight integrated SEDs for dense molecular cloud structures using radiative transfer with physically plausible density and temperature distributions for the MC material, AME spectra with peaks at $\nu < 50$ GHz are obtained.

4.4. Dust Emission

An alternate explanation for the higher emissivity we see at 3 mm and 1 cm is that the dust itself has intrinsically higher emissivity at long wavelengths compared to what would be expected based on the MBB extrapolation from shorter-wavelength data. An attractive feature of this model is that it naturally explains the excellent correspondence seen between the morphology of the 3 mm map and the shorter-wavelength maps. It also explains the presence of enhanced emissivity in the full range of environments studied here—optically thick free–free, for instance, cannot explain the long-wavelength excess that is observed in the filament itself.

Intriguingly, the *Planck* data shown in Figure 3 of S14 hint at a flattening spectrum at $\lambda > 4$ mm similar to that seen here. The evidence is inconclusive owing to *Planck*'s very different spatial frequency filtering and low angular resolution compared to the scale of the structures being studied: 10′–33′, for *Planck* measurements between 100 GHz and 31 GHz, respectively, as opposed to the 25″–3′ scales studied here. The effects of beam dilution on the SED derived from *Planck* data will also vary considerably with frequency over the range of interest. The *Planck* collaboration (Planck Collaboration et al. 2014) do find that a single β MBB fit from 353 to 3000 GHz, extrapolated down to 100 GHz, also underpredicts the observed *Planck* dust emission. Meisner & Finkbeiner (2015) fit this data to a two-component graybody model and are able to accurately predict the 100 GHz emission. The measurements reported here suggest that this flattened spectrum continues to a wavelength of 1 cm.

Detailed models of emission from amorphous dust grains based on laboratory measurements predict a flattened spectrum (higher emissivity) at long wavelengths (Meny et al. 2007; Coupeaud et al. 2011; Paradis et al. 2011), mainly due to two-level system fluctuations in the dust grains. Figure 8 shows that while this model could help explain the 3 mm data points, it underpredicts the 1 cm emissivity. Thus, multiple factors could be relevant to the data we present here.

5. Conclusions

We have presented sensitive, new 3 mm and 1 cm continuum measurements of the "integral-shaped filament", OMC 2/3. These measurements confirm the enhanced 3 mm brightness of OMC 2/3 first reported in Schnee et al. (2014), and support similar findings at lower resolution throughout the Galaxy as a whole (e.g., Planck Collaboration et al. 2014; Meisner & Finkbeiner 2015). Our data indicate that this finding extends to very dense MC environments and potentially to frequencies as low as 30 GHz. Consistent with Sadavoy et al. (2016), we find that the data from 2 mm to 160 μm are in contrast well described by a simple MBB with $\beta \sim 1.6$. This supports the suggestion advanced by S16 that there may be a deviation from a simple MBB SED at long wavelengths. If the long-wavelength data are empirically modeled by allowing a break in the spectrum at 120 GHz, the 1 cm–3 mm spectrum corresponds to $\beta' \sim 0.7$. The long-wavelength emissivity index β' is generally consistent in most of the regions studied (filament, protostellar core, and regions with a known free–free source), but significantly flatter in the five starless cores studied here, with $\beta' = 0.20 \pm 0.06$.

Some models of radiation from amorphous dust grains do predict enhanced long-wavelength brightness (Meny et al. 2007; Coupeaud et al. 2011; Paradis et al. 2011). This explanation would naturally explain the excellent correspondence of the 3 mm continuum maps with the morphology seen at shorter wavelengths. While this model may explain much of the observed 3 mm brightness, it appears to underpredict the 1 cm signal. Canonical AME models do not provide a good fit to the observed long-wavelength spectrum, but could account for the 1 cm signal. In some of our target regions, particularly those with known protostars, we cannot rule out a contribution from thermal Bremsstrahlung that is optically thick up to a turnover frequency at $\nu > 31$ GHz. The spectra of *known* free–free regions in OMC 2/3, however, provides no evidence for such a scenario. Free–free cannot account for the observed long-wavelength SED in the filament itself, and is unlikely to do so in starless cores.

In spite of the relative faintness of dust emission at 3 mm, interferometric surveys of known star-forming regions are common at this wavelength (e.g., Carpenter 2002; Eisner & Carpenter 2006; Dunham et al. 2016; Kainulainen et al. 2017; Kirk et al. 2017). In part this is due to the relatively large fields of view and higher instrumental sensitivity that interferometers provide at these lower wavelengths. The data from such surveys are also less affected by optical depth considerations than shorter-wavelength data. Our findings could have substantial implications on the interpretation of data from 3 mm core surveys, suggesting that masses and densities of cores determined from them could be overestimated by a factor of 2–3. Such an overestimate would correspondingly impact dynamical stability estimates of the cores made from 3 mm measurements. In order to interpret these surveys reliably, and to conclusively understand the physical conditions in this region and regions like it, high-quality observations at intermediate and lower frequencies will be needed as well as more detailed modeling of the dust and ISM conditions.

Sara Stanchfield was supported by NASA NSTRF NNX14AN63H. Other investigators at the University of Pennsylvania were supported by NSF grant 1615604, and by the Mt. Cuba Astronomical Foundation. We thank Diego Mardones, Di Li, and Jeremy Ren for sharing their ALMA data; Scott Schnee, Dana Balser, Loren Anderson, and Remy Indebetouw for insightful comments about the scientific interpretation of the data we present; Luca Di Mascolo for expert advice on AplPy; Johannes Staguhn for providing the GISMO bandpass; and Bryan Butler for providing the VLA data on 3C138 which facilitated calibrating our *Ka*-band GBT data. The National Radio Astronomy Observatory and the Green Bank Observatory are facilities of the National Science Foundation operated under cooperative agreement by Associated Universities, Inc. This paper makes use of the following ALMA data: ADS/JAO.ALMA#2013.0.00662. S. ALMA is a partnership of ESO (representing its member states), NSF (USA), and NINS (Japan), together with NRC (Canada), MOST and ASIAA (Taiwan), and KASI (Republic of Korea), in cooperation with the Republic of Chile. The Joint ALMA Observatory is operated by ESO, AUI/NRAO, and NAOJ.

Facilities: GBT, VLA, ALMA, IRAM:30m, Herschel, JCMT.

Software: AplPy (Robitaille & Bressert 2012), Astropy (Astropy Collaboration et al. 2013), CASA (McMullin et al. 2007), ds9 (Joye & Mandel 2003).

ORCID iDs

Brian Mason https://orcid.org/0000-0002-8472-836X
Sarah Sadavoy https://orcid.org/0000-0001-7474-6874
Tony Mroczkowski https://orcid.org/0000-0003-3816-5372
Charles Romero https://orcid.org/0000-0001-5725-0359
Rachel Friesen https://orcid.org/0000-0001-7594-8128
Craig Sarazin https://orcid.org/0000-0003-0167-0981
Jonathan Sievers https://orcid.org/0000-0001-6903-5074
Thomas Stanke https://orcid.org/0000-0002-5812-9232
Mark Devlin https://orcid.org/0000-0002-3169-9761

References

Ali-Haïmoud, Y., Hirata, C. M., & Dickinson, C. 2009, MNRAS, 395, 1055
Astropy Collaboration, Robitaille, T. P., & Tollerud, J. E. 2013, A&A, 558, A33
Carpenter, J. M. 2002, AJ, 124, 1593
Condon, J. J., Cotton, W. D., Greisen, E. W., et al. 1998, AJ, 115, 1693
Coupeaud, A., Demyk, K., Meny, C., et al. 2011, A&A, 535, A124
Davis, C. J., Froebrich, D., Stanke, T., et al. 2009, A&A, 496, 153
de Oliveira-Costa, A., Kogut, A., Devlin, M. J., et al. 1997, ApJL, 482, L17
Dicker, S. R., Ade, P. A. R., Aguirre, J., et al. 2014, JLTP, 176, 808
Dickinson, C., Ali-Haïmoud, Y., Barr, A., et al. 2018, NewAR, 80, 1
Draine, B. T., & Lazarian, A. 1998, ApJ, 508, 157
Draine, B. T., & Lazarian, A. 1999, ApJ, 512, 740
Dunham, M. M., Offner, S. S. R., Pineda, J. E., et al. 2016, ApJ, 823, 160
Eisner, J. A., & Carpenter, J. M. 2006, ApJ, 641, 1162
Finkbeiner, D. P., Langston, G. I., & Minter, A. H. 2004, ApJ, 617, 350
Fomalont, E., van Kempen, T., Kneissl, R., et al. 2014, Msngr, 155, 19
Frayer, D. T., Maddalena, R. J., White, S., et al. 2019, arXiv:1906.02307
Friesen, R. K., Pineda, J. E., Rosolowsky, E., et al. 2017, arXiv:1704.06318
Goldsmith, P. F., Bergin, E. A., & Lis, D. C. 1997, ApJ, 491, 615
Greaves, J. S., Scaife, A. M. M., Frayer, D. T., et al. 2018, NatAs, 2, 662
Hoang, T., Vinh, N.-A., & Quynh Lan, N. 2016, ApJ, 824, 18
Hunter, T. R., Schwab, F. R., White, S. D., et al. 2011, PASP, 123, 1087
Johnstone, D., & Bally, J. 1999, ApJL, 510, L49
Jørgensen, J. K., Johnstone, D., van Dishoeck, E. F., & Doty, S. D. 2006, A&A, 449, 609
Joye, W. A., & Mandel, E. 2003, in ASP Conf. Ser. 295, Astronomical Data Analysis Software and Systems XII, ed. H. E. Payne, R. I. Jedrzejewski, & R. N. Hook (San Francisco, CA: ASP), 489
Kainulainen, J., Stutz, A. M., Stanke, T., et al. 2017, A&A, 600, A141
Kirk, H., Dunham, M. M., Di Francesco, J., et al. 2017, ApJ, 838, 114
Kogut, A., Banday, A. J., Bennett, C. L., et al. 1996, ApJL, 464, L5
Leitch, E. M., Readhead, A. C. S., Pearson, T. J., & Myers, S. T. 1997, ApJL, 486, L23
Mairs, S., Johnstone, D., Kirk, H., et al. 2016, MNRAS, 461, 4022
Mason, B. S., Weintraub, L., Sievers, J., et al. 2009, ApJ, 704, 1433
McMullin, J. P., Waters, B., Schiebel, D., Young, W., & Golap, K. 2007, in ASP Conf. Ser. 376, Astronomical Data Analysis Software and Systems XVI, ed. R. A. Shaw, F. Hill, & D. J. Bell (San Francisco, CA: ASP), 127
Megeath, S. T., Gutermuth, R., Muzerolle, J., et al. 2016, AJ, 151, 5
Meisner, A. M., & Finkbeiner, D. P. 2015, ApJ, 798, 88
Meny, C., Gromov, V., Boudet, N., et al. 2007, A&A, 468, 171
Murphy, E. J., Helou, G., Condon, J. J., et al. 2010, ApJL, 709, L108
Murphy, E. J., Linden, S. T., Dong, D., et al. 2018, ApJ, 862, 20
Nikolic, B., Prestage, R. M., Balser, D. S., Chandler, C. J., & Hills, R. E. 2007, A&A, 465, 685
Nutter, D., & Ward-Thompson, D. 2007, MNRAS, 374, 1413
Paradis, D., Bernard, J.-P., Mény, C., & Gromov, V. 2011, A&A, 534, A118
Peterson, D. E. 2005, PhD thesis, Univ. Rochester, New York
Planck Collaboration, Abergel, A., Ade, P. A. R., et al. 2014, A&A, 571, A11
Planck Collaboration, Ade, P. A. R., Aghanim, N., et al. 2011, A&A, 536, A20
Planck Collaboration, Ade, P. A. R., Alves, M. I. R., et al. 2015, A&A, 576, A107
Reipurth, B., Rodríguez, L. F., & Chini, R. 1999, AJ, 118, 983
Robitaille, T., & Bressert, E. 2012, APLpy: Astronomical Plotting Library in Python, Astrophysics Source Code Library, ascl:1208.017
Romero, C. E., Sievers, J., Ghirardini, V., et al. 2019, arXiv:1908.09200
Sadavoy, S. I., Di Francesco, J., Bontemps, S., et al. 2010, ApJ, 710, 1247
Sadavoy, S. I., Di Francesco, J., Johnstone, D., et al. 2013, ApJ, 767, 126
Sadavoy, S. I., Stutz, A. M., Schnee, S., et al. 2016, A&A, 588, A30

Salji, C. J., Richer, J. S., Buckle, J. V., et al. 2015, MNRAS, 449, 1782
Schnee, S., Mason, B., Di Francesco, J., et al. 2014, MNRAS, 444, 2303
Silsbee, K., Ali-Haïmoud, Y., & Hirata, C. M. 2011, MNRAS, 411, 2750
Simón-Díaz, S., García-Rojas, J., Esteban, C., et al. 2011, A&A, 530, A57
Smith, J., Harper, D. A., & Loewenstein, R. F. 1987, ApJ, 314, 76
Stanchfield, S. M., Ade, P. A. R., Aguirre, J., et al. 2016, JLTP, 184, 460
Stutz, A. M., & Kainulainen, J. 2015, A&A, 577, L6
van Kempen, T., Kneissl, R., Marcelino, N., et al. 2014, ALMA Memo, 599, https://library.nrao.edu/public/memos/alma/main/memo599.pdf
Ysard, N., Juvela, M., & Verstraete, L. 2011, A&A, 535, A89